Table 3
Adverse events.

	TACE group						TAI group					
	Grade 3		Grade 4		Grade 1–4		Grade 3		Grade 4		Grade 1–4	
	No.	%	No.	%	No.	%	No.	%	No.	%	No.	%
Hematological toxicity												
Leukocytes	1	1	0	0	27	34	0	0	0	0	26	32
Neutrophils	1	0	0	0	14	18	0	0	0	0	15	18
Hemoglobin	1	1	–		25	32	0	0	–		23	28
Platelets	10	13	2	3	54	68	10	12	3	4	57	70
Non-hematological toxicity												
Total bilirubin	21	27	0	0	60	76	15	18	0	0	62	76
Alkaline phosphatase	2	3	0	0	53	67	2	2	0	0	63	77
Aspartate aminotransferase	33	42	0	0	77	97	23	28	0	0	79	96
Alanine aminotransferase	28	35	0	0	73	92	16	20	0	0	77	94
Creatinine	0	0	0	0	13	16	0	0	0	0	16	20
Abdominal pain	0	0	0	0	55	70	2	2	0	0	50	61
Nausea/vomiting	1	1	–		43	54	0	0	–		39	48
Diarrhea	0	0	0	0	2	3	0	0	0	0	4	5
Fever	2	3	0	0	69	87	1	1	0	0	66	80
Shivers	0	0	0	0	12	15	1	1	0	0	14	17
Allergy	0	0	0	0	2	3	0	0	0	0	6	7
Ascites	1	1	–		3	4	0	0	–		0	0
Dyspnea	0	0	0	0	0	0	0	0	1	1	1	1
Hypotension	1	1	0	0	1	1	1	1	0	0	1	1

A 'dash' (–) indicates the grade was not available.

phatic drainage from the tumor interstitium, macromolecular agents like SMANCS are retained more selectively within tumors [24,25]. In fact, experimental studies have shown that tumor-systemic drug concentration ratios as high as 1000 can be achieved using TAI with SMANCS-lipiodol. Thus, the selective delivery of a long-lasting or slow-release anti-cancer agent may have had a sufficient antitumor effect and survival-prolonging efficacy in the TAI group even if embolization had not been used in combination.

The infrequent protocol treatment repetition in this study is another possible reason for the lack of any difference in survival between the two groups, because the average number of protocol treatments was only 2.2 courses in the TACE group and 2.4 in the TAI group, and thus the maximum anti-cancer potential may not have been achieved. We speculated that the choice of SMANCS was partly responsible for the infrequent repetition because hepatic vascular complications, such as the obstruction of the hepatic artery and the arterio-portal shunt, have been reported as adverse reactions specific to SMANCS [26]. These complications are often followed by liver dysfunction, ascites, and technical problems with regard to subsequent protocol treatment, which were the major reasons for treatment discontinuation in this study. The enrollment of many patients with far-advanced HCC in the present phase III study may have been another reason for the small number of treatment repetitions and the subsequent poor survival: the proportion of patients with a pre-treatment AFP level >200 ng/mL was 40% in the phase III study and

24% in the phase II study. Both the antitumor response and the overall survival of the TACE group were poorer than our expectations: the 2-year survival rate in the TACE group was 48.2% in the present study, as opposed to 79% in the phase II study of TACE with SMANCS.

In conclusion, the results of this study suggest that treatment intensification by adding embolization did not increase the survival of HCC patients over SMANCS transarterial chemotherapy alone. The results of this study also showed no significant differences in toxicity, except for an ALP elevation, between the two groups treated with SMANCS. It should be emphasized that the negative results in this study may be attributable to our methodological strategy for selecting SMANCS and the enrollment of many patients with far-advanced HCC. The infrequent treatment repetition and the favorable results of TAI with SMANCS are speculated to be reasons for the lack of any difference in survival between the two groups. Furthermore, the results of this study must be interpreted with caution because current TACE protocols have evolved thanks to the implementation of updated devices including new embolic agents and improved catheters. Additional studies will be required to determine whether the results obtained in this trial are consistent with the results of transarterial treatment with chemotherapeutic agents other than SMANCS and with updated procedures, although it would be difficult to conduct such studies because many consider TACE to be the standard treatment based on the positive results obtained in two recent randomized studies in which doxorubicin or cisplatin was used

[7,8]. There is a more pressing need for the establishment of new and more active treatment strategies that are superior to conventional TACE to improve the dismal prognosis of this disease.

Acknowledgments

References

[1] Bosch FX, Ribes J, Cléries R, Díaz M. Epidemiology of hepatocellular carcinoma. Clin Liver Dis 2005;9:191–211.

[2] Lin DY, Liaw YF, Lee TY, Lai CM. Hepatic arterial embolization in patients with unresectable hepatocellular carcinoma – a randomized controlled trial. Gastroenterology 1988;94:453–456.

[3] Pelletier G, Roche A, Ink O, Anciaux ML, Derhy S, Rougier P, et al. A randomized trial of hepatic arterial chemoembolization in patients with unresectable hepatocellular carcinoma. J Hepatol 1990;11:181–184.

[4] Groupe d'Etude et de Traitement du Carcinome Hépatocellulaire. A comparison of lipiodol chemoembolization and conservative treatment for unresectable hepatocellular carcinoma. N Engl J Med 1995;332:1256–61.

[5] Pelletier G, Ducreux M, Gay F, Luboinski M, Hagège H, Dao T, et al. Treatment of unresectable hepatocellular carcinoma with lipiodol chemoembolization: a multicenter randomized trial. Groupe CHC. J Hepatol 1998;29:129–134.

[6] Bruix J, Llovet JM, Castells A, Montañá X, Brú C, Ayuso MC, et al. Transarterial embolization versus symptomatic treatment in patients with advanced hepatocellular carcinoma: results of a randomized, controlled trial in a single institution. Hepatology 1998;27:1578–1583.

[7] Lo CM, Ngan H, Tso WK, Liu CL, Lam CM, Poon RT, et al. Randomized controlled trial of transarterial lipiodol chemoembolization for unresectable hepatocellular carcinoma. Hepatology 2002;35:1164–1171.

[8] Llovet JM, Real MI, Montaña X, Planas R, Coll S, Aponte J, et al. Arterial embolisation or chemoembolisation versus symptomatic treatment in patients with unresectable hepatocellular carcinoma: a randomised controlled trial. Lancet 2002;359:1734–1739.

[9] Doffoel M, Vetter D, Bouche O, Bonnetain F, Abergel A, Fratte S, et al. Multicenter randomized phase III trial comparing tamoxifen alone or with transarterial lipiodol chemoembolization (TLC) for unresectable hepatocellular carcinoma (HCC) in cirrhotic patients (Abstract). J Clin Oncol 2005;23:4006.

[10] Cammà C, Schepis F, Orlando A, Albanese M, Shahied L, Trevisani F, et al. Transarterial chemoembolization for unresec-table hepatocellular carcinoma: meta-analysis of randomized controlled trials. Radiology 2002;224:47–54.

[11] Llovet JM, Bruix J. Systematic review of randomized trials for unresectable hepatocellular carcinoma: chemoembolization improves survival. Hepatology 2003;37:429–442.

[12] Konno T, Maeda H, Iwai K, Tashiro S, Maki S, Morinaga T, et al. Effect of arterial administration of high-molecular-weight anticancer agent SMANCS with lipid lymphographic agent on hepatoma: a preliminary report. Eur J Cancer Clin Oncol 1983;19:1053–1065.

[13] Okusaka T, Okada S, Ishii H, Ikeda M, Nakasuka H, Nagahama H, et al. Transarterial chemotherapy with zinostatin stimalamer for hepatocellular carcinoma. Oncology 1998;55:276–283.

[14] Liver Cancer Study Group of Japan. Criteria for evaluation of direct effects on hepatocellular carcinoma. Kanzo 1994;35: 193–205.

[15] Bruix J, Sherman M, Llovet JM, Beaugrand M, Lencioni R, Burroughs AK, et al. Clinical management of hepatocellular carcinoma. Conclusions of the Barcelona-2000 EASL conference. European Association for the Study of the Liver. J Hepatol 2002;35:421–430.

[16] Takayasu K, Arii S, Matsuo N, Yoshikawa M, Ryu M, Takasaki K, et al. Comparison of CT findings with resected specimens after chemoembolization with iodized oil for hepatocellular carcinoma. Am J Roentgenol 2000;175:699–704.

[17] Okusaka T, Okada S, Ueno H, Ikeda M, Yoshimori M, Shimada K, et al. Evaluation of the therapeutic effect of transcatheter arterial embolization for hepatocellular carcinoma. Oncology 2000;58:293–299.

[18] Japan society for cancer therapy: toxicity grading criteria of the Japan society for cancer therapy. J Jpn Soc Cancer Ther 1997; 32:61–5.

[19] World Health Organization. WHO handbook for reporting results of cancer treatment; offset publication 48. Geneva: World Health Organization; 1979.

[20] Okusaka T, Okada S, Ueno H, Ikeda M, Iwata R, Furukawa H, et al. Transcatheter arterial embolization with zinostatin stimal-amer for hepatocellular carcinoma. Oncology 2002;62:228–233.

[21] Kirchhoff TD, Bleck JS, Dettmer A, Chavan A, Rosenthal H, Merkesdal S, et al. Transarterial chemoembolization using degradable starch microspheres and iodized oil in the treatment of advanced hepatocellular carcinoma: evaluation of tumor response, toxicity, and survival. Hepatobiliary Pancreat Dis Int 2007;6:259–266.

[22] Maeda H, Takeshita J, Kanamaru R. A lipophilic derivative of neocarzinostatin. A polymer conjugation of an antitumor protein antibiotic. Int J Pept Protein Res 1979;14:81–87.

[23] Maeda H, Takeshita J, Kanamura R, Sato H, Khatoh J, Sato H. Antimetastatic and antitumor activity of a derivative of neocarzi-nostatin: an organic solvent- and mater-soluble polymerconjugat-ed protein. Gann 1979;70:601–606.

[24] Iwai K, Maeda H, Konno T. Use of oily contrast medium for selective drug targeting to tumor: enhanced therapeutic effect and X-ray image. Cancer Res 1984;44:2115–2121.

[25] Iwai K, Maeda H, Konno T, Matsumura Y, Yamashita R, Yamasaki K, et al. Tumor targeting by arterial administration of lipids: rabbit model with VX2 carcinoma in the liver. Anticancer Res 1987;7:321–327.

[26] Ikeda K, Saitoh S, Kobayashi M, Suzuki Y, Suzuki F, Tsubota A, et al. Hepatic vascular side effects of styrene maleic acid neocarzinostatin in the treatment of hepatocellular carcinoma. J Gastroenterol 2000;35:353–360.

Original Article

Real-Time Identification of Liver Cancers by Using Indocyanine Green Fluorescent Imaging

Takeaki Ishizawa, MD[1], Noriyoshi Fukushima, MD, PhD[2], Junji Shibahara, MD, PhD[2], Koichi Masuda, MD[1], Sumihito Tamura, MD[1], Taku Aoki, MD, PhD[1], Kiyoshi Hasegawa, MD, PhD[1], Yoshifumi Beck, MD, PhD[1], Masashi Fukayama, MD, PhD[2], and Norihiro Kokudo, MD, PhD[1]

BACKGROUND: We have often encountered difficulties in identifying small liver cancers during surgery. Fluorescent imaging using indocyanine green (ICG) has the potential to detect liver cancers through the visualization of the disordered biliary excretion of ICG in cancer tissues and noncancerous liver tissues compressed by the tumor. **METHODS:** ICG had been intravenously injected for a routine liver function test in 37 patients with hepatocellular carcinoma (HCC) and 12 patients with metastasis of colorectal carcinoma (CRC) before liver resection. Surgical specimens were investigated using a near-infrared light camera system. Among the 49 subjects, the 26 patients examined during the latter period of the study (20 with HCC and 6 with metastasis) underwent ICG-fluorescent imaging of the liver surfaces before resection. **RESULTS:** ICG-fluorescent imaging identified all of the microscopically confirmed HCCs (n = 63) and CRC metastases (n = 28) in surgical specimens. Among the 63 HCCs, 8 tumors (13%, including 5 early HCCs) were not evident grossly unless observed by ICG-fluorescent imaging. Five false-positive nodules (4 large regenerative nodules and 1 bile duct proliferation) were identified among the fluorescent lesions. Well-differentiated HCCs appeared as uniformly fluorescing lesions with higher lesion-to-liver contrast than that of moderately or poorly differentiated HCCs (162.6 [71.1-218.2] per pixel vs 67.7 [-6.3-211.2] per pixel, P < .001), while CRC metastases were delineated as rim-fluorescing lesions. Fluorescent microscopy confirmed that fluorescence originated in the cytoplasm and pseudoglands of HCC cells and in the noncancerous liver parenchyma surrounding metastases. ICG-fluorescent imaging before resection identified 21 of the 41 HCCs (51%) and all of the 16 metastases that were examined. **CONCLUSIONS:** ICG-fluorescent imaging enables the highly sensitive identification of small and grossly unidentifiable liver cancers in real time, enhancing the accuracy of liver resection and operative staging. **Cancer 2009;115:2491-504.** © **2009 American Cancer Society.**

KEY WORDS: hepatocellular carcinoma, early hepatocellular carcinoma, liver metastasis, liver resection, diagnosis.

Although liver resection has played a leading role in the treatment of hepatocellular carcinoma (HCC) and metastases of colorectal carcinoma (CRC), the intraoperative diagnosis of small tumors

Table 1. Patients' Background Characteristics

Variable	HCC, n=37	Metastasis of CRC, n=12
Age, y*	67 (22-79)	64 (52-73)
ICG retention rate at 15 minutes (%)*	13.9 (3.7-46.5)	7.4 (2.2-13.0)
Child-Pugh class, A/B (%)	34 (92)/3 (8)	12 (100)/0 (0)
Hepatitis B virus surface antigen, positive/negative (%)	12 (32)/25 (68)	0 (0)/12 (100)
Hepatitis C virus antibody, positive/negative (%)	14 (38)/23 (62)	0 (0)/12 (100)
Background liver, cirrhosis/noncirrhosis (%)	12 (32)/25 (68)	0 (0)/12 (100)

HCC indicates hepatocellular carcinoma; CRC, colorectal carcinoma; ICG, indocyanine green.
* Median with range.

remains insufficient. Despite recent advances in imaging modalities, 3%-17% of HCCs[1,2] and metastases of CRC[1,3-5] can be detected only by microscopic examinations. In particular, we have often encountered difficulties in identifying small (< 2.0 cm) HCCs with indistinct margins (early HCC[6-9] or very early HCC[10]). Such grossly unidentifiable liver cancers may be overlooked by operative or even pathological diagnosis because thorough microscopic examinations of entire specimens are practically unfeasible. Novel intraoperative imaging techniques are needed to enhance the accuracy of liver resection and the pathological diagnosis of small liver cancers.

Recently, fluorescent imaging techniques using indocyanine green (ICG) have been used to assess coronary artery bypass graft patency during surgery.[11,12] These techniques are based on the finding that ICG binds to plasma proteins and protein-bound ICG emits light with a peak wavelength of around 830 nm when illuminated with near-infrared light.[13] Initially, we tried to apply fluorescent imaging techniques to intraoperative cholangiography.[14] While performing intraoperative cholangiography procedures in HCC patients, we happened to discover that HCCs fluoresced strongly even before the intrabiliary injection of ICG for cholangiography. Because these patients had received an intravenous injection of ICG for a routine liver function test before surgery and intravenously injected ICG is excreted exclusively by the liver,[15] we hypothesized that the HCCs fluoresced because they had retained the preoperatively injected ICG as a result of biliary excretion disorders in the cancerous tissues. Such fortuitous experiences have led us to develop the novel fluorescent imaging techniques described in this article; these techniques enable the highly sensitive identification of liver cancers through the visualization of the

disordered biliary excretion of ICG that exists in HCC and noncancerous liver tissues surrounding CRC metastases.

MATERIALS AND METHODS

Patients

The subjects comprised 49 patients who had undergone liver resection for HCC (n = 37) or CRC metastasis (n = 12) at the University of Tokyo Hospital during the months between July and September 2007 and in March 2008, when a fluorescent imaging system was available at the hospital. Among the patients with HCC, the ICG retention rate at 15 minutes ranged from 3.7% to 46.5% (median, 13.9%) and 3 Child-Pugh class B patents were included, whereas the patients with metastases had normal liver function (Table 1).

Before surgery, all patients underwent abdominal ultrasonography and contrast-enhanced helical computed tomography (CT) examinations. In patients with HCC, resection was indicated for tumors in which the CT examination revealed both early hyperenhancement and delayed hypoenhancement.[7,16] During surgery, the liver was evaluated by visual inspection, manual palpation, and intraoperative ultrasonography.[17] Newly detected HCCs or metastases were resected whenever possible.[17,18]

ICG-Fluorescent Imaging of Surgical Specimens and Subsequent Pathological Examinations

As a fluorescent source, we used ICG (Diagnogreen, Daiichi Sankyo, Tokyo, Japan), which had been

intravenously injected before surgery at a dose of 0.5 mg per kg of body weight as part of a routine liver function test to determine the operative indications and procedures.[16,19] The intervals between the ICG injection and surgery ranged from 1 to 7 days (median, 3 days) in patients with HCC and from 1 to 14 days (median, 3 days) in patients with metastasis.

Surgical specimens were cut to include each tumor's maximum diameter based on gross inspection immediately after liver resection. The remaining parts of the specimens were also sliced into 10-mm sections using a long blade. All of the cut surfaces were grossly examined and subsequently investigated using the fluorescent imaging system in the operation room, without referring to the pre- or intraoperative findings. Any fluorescing lesions were marked with needles for subsequent microscopic examination if they were larger than 5 mm in size, because routine pathological examinations to discriminate small liver cancer from large regenerative nodules or dysplastic nodules are often performed for lesions with a diameter of greater than 5 mm.[20]

All the surgical specimens were formalin fixed and examined by experienced pathologists (N.F. and J.S.). All grossly identified nodules were microscopically evaluated irrespective of the presence or absence of ICG-fluorescence. A diagnosis of HCC was made according to the Japanese classification system[8] and the criteria proposed by the International Working Party.[20] The definition of early HCC was as follows: grossly, the tumor exhibits indistinct margins and does not destroy the preexisting hepatic framework; microscopically, it comprises uniformly distributed well-differentiated cancerous tissues with little cellular and architectural atypia and grows at tumor-nontumor boundaries as if it is replacing the neighboring liver cell cords.[6-9]

Fluorescent Imaging System

The fluorescent imaging system (PDE, Hamamatsu Photonics, Hamamatsu, Japan) comprised a small control unit (322 × 283 × 55 mm) and a camera unit (80 × 181 × 80 mm). The camera unit comprised a charge-coupled device camera, which filtered out light with a wavelength below 820 nm, and 36 light emitting diodes with a wavelength of 760 nm. The camera imaging head was positioned 20 cm above the surgical specimen,

which was set in a lightproof box, with the output of light emitting diodes set at 1 mW per cm^2. Data were transmitted to a personal computer via an image capture card, and fluorescent images were created and stored at 72 pixels per inch.

Measurement of Signal Intensity on Fluorescent Images

The signal intensities of the lesions and noncancerous liver tissues were determined by calculating the mean brightness of an operator-defined region of interest on monochromatic fluorescent images of surgical specimens with the help of Photoshop version 7.0 software (Adobe Systems, San Jose, Calif). The brightness of each pixel was measured within a range of 0-255. The lesion-to-liver contrast was calculated by subtracting the signal intensity of the noncancerous liver parenchyma from that of the lesion.

Fluorescent Microscopy

Surgical specimens were fixed with formalin, sectioned at 10 μm, and stained with hematoxylin only (eosin was avoided because of the fluorescence of the dye itself). Fluorescent microscopic examinations were performed using an upright epifluorescence microscope (Eclipse 55i with a J-FL attachment, Nikon Instruments, Tokyo, Japan) with a cooled charge-coupled device camera (Retiga EXi, QImaging, Surrey, BC, Canada), a xenon light source (MAX-302, Asahi Spectra, Tokyo, Japan), and filters (excitation 775 ± 50 nm and emission 810 nm longpass and 845 ± 55 nm bandpass, Chroma Technology, Rockingham, Vt).

ICG-Fluorescent Imaging Before Resection

Among the 49 subjects, the latter 26 patients (20 with HCC and 6 with CRC metastases) underwent ICG-fluorescent imaging before resection: After the mobilization of the liver, the camera imaging head was positioned 20 cm above the liver surface (the output of the light emitting diodes was 4 mW per cm^2), the surgical lights were turned off (the ceiling lights were kept on), and the fluorescent images on the liver surfaces were displayed on a television monitor in the operation room.

Table 2. Characteristics of the Lesions Detected Only by Indocyanine Green-Fluorescent Imaging

Case	ICG Retention Rate at 15 Minutes, %	Child-Pugh Class	Preoperative Diagnosis*	Intraoperative Ultrasonography	Tumor Size, mm	Microscopic Diagnosis
1	8.0	A	HCC	ND	2	Moderately differentiated HCC
2	4.8	A	HCC	Hyperechoic	4	Well-differentiated HCC
3	26.4	B	ND	ND	12	Well-differentiated HCC
4	17.1	A	ND	Hypoechoic	19	Early HCC
5	3.8	A	ND	Hypoechoic	12	Early HCC
5	3.8	A	ND	ND	10	Early HCC
6	15.1	A	ND	ND	8	Early HCC
7	9.8	A	ND	ND	6	Early HCC
8	20.7	A	ND	Hyperechoic	7	Large regenerative nodule
9	23.4	A	ND	ND	7	Large regenerative nodule
3	26.4	B	ND	ND	6	Large regenerative nodule
10	21.3	A	ND	Hyperechoic	5	Large regenerative nodule
11	15.1	A	ND	ND	5	Bile duct proliferation

ICG indicates indocyanine green; HCC, hepatocellular carcinoma; ND, not detected.
*According to ultrasonography and contrast-enhanced helical computed tomography.

Statistical Analysis

Continuous data are expressed as the median (range). Categorical data and continuous data were compared using a Fisher exact test and the Wilcoxon rank sum test, respectively. We assigned statistical significance at $P < .05$. The calculations were performed with the help of JMP version 5.1.1 software (SAS Institute, Cary, NC).

RESULTS

Cancer Detection by Using ICG-Fluorescent Imaging of Surgical Specimens

Microscopic examinations confirmed a total of 91 cancers (63 HCCs and 28 metastases of CRC). All of the HCCs and metastases were identified using our ICG-fluorescent imaging technique on the cut surfaces of the surgical specimens.

Table 2 summarizes the 13 lesions that were detected using ICG-fluorescent imaging technique but that were not evident during gross examination of the cut surfaces of the specimens. These 13 lesions comprised 8 HCCs (13% of the 63 HCCs, Fig. 1), including 5 early HCCs (45% of the 11 early HCCs in our series, Fig. 2), and 5 false-positive nodules (4 large regenerative nodules and 1 bile duct proliferation). Our series also included 10 nonfluorescent nodules (found in 6 patients with HCC), which microscopically proved to be regenerative nodules (n = 8) and dysplastic nodules (n = 2). All 28 CRC me-

tastases were identified by both gross examination and fluorescent imaging.

The sensitivities and positive predictive values of the ICG-fluorescent imaging on surgical specimens for HCC were thus 100% and 93% (63 cancers of the 68 fluorescing lesions), respectively, while those for the CRC metastases were 100% and 100%, respectively.

Fluorescent Patterns of Liver Cancers

The fluorescent patterns of the 63 HCCs on the cut surfaces of the surgical specimens were classifiable into the following 3 types: a total fluorescent type (all of the cancer tissues showed a uniform fluorescence, n = 33, Fig. 3A), a partial fluorescent type (part of the cancer tissues showed fluorescence, n = 26, Fig. 3B), and a rim fluorescent type (the cancer tissues were negative for fluorescence but the surrounding liver parenchyma showed fluorescence, n = 4, Fig. 3C). All of the 28 CRC metastases displayed rim fluorescence (Fig. 3D).

Between the total fluorescent-type HCCs and the partial-fluorescent-type HCCs, the former group comprised smaller tumors (12^{2-40} mm vs 30^{7-150} mm; $P = .001$) and, microscopically, well-differentiated carcinomas and pseudogland formation were more common among the total fluorescent-type HCCs (58% vs 0%; $P < .001$, and 85% vs 50%; $P = .005$, respectively; Table 3). The rim fluorescent-type HCCs comprised only poorly differentiated carcinomas.
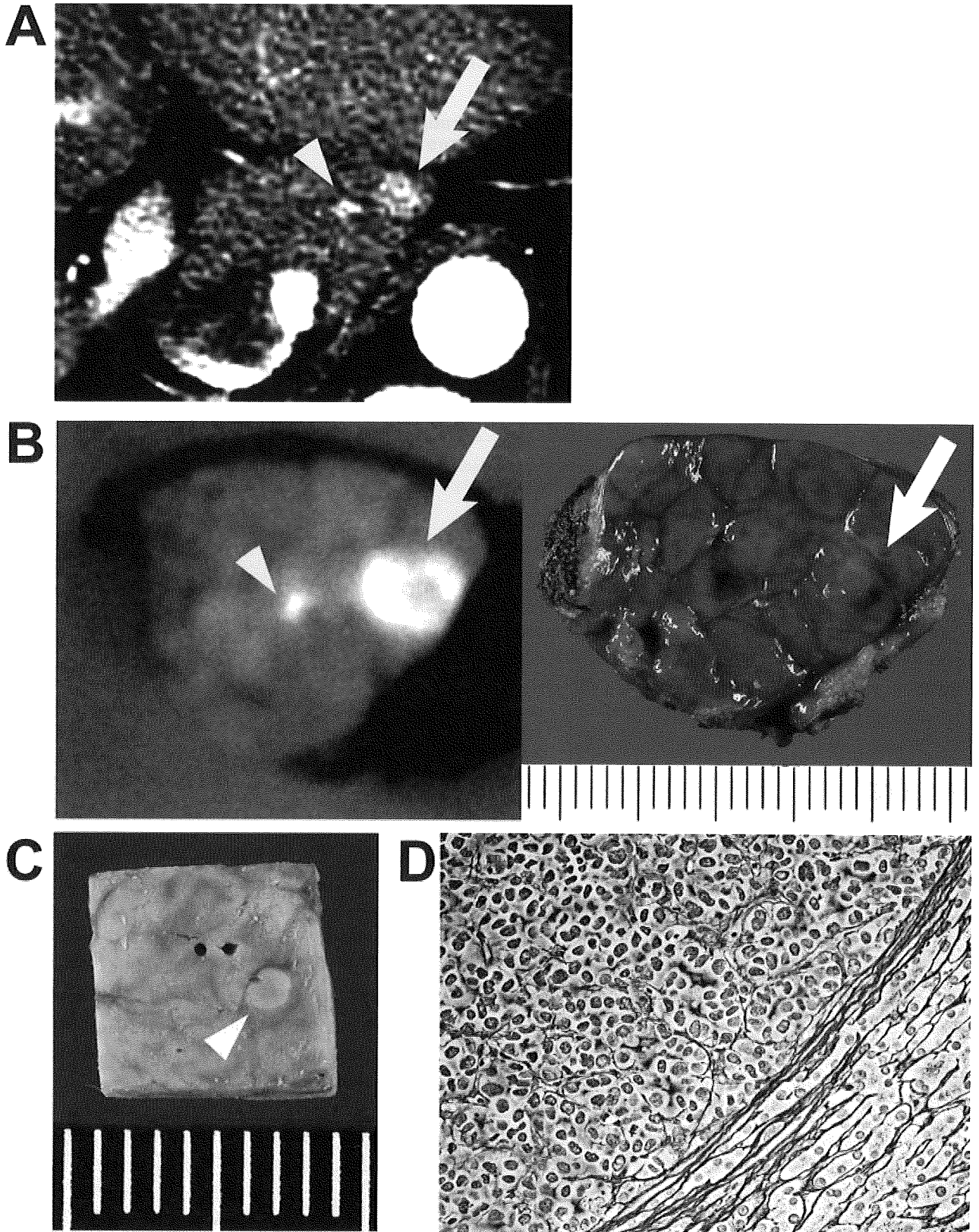
FIGURE 1. Hepatocellular carcinomas that were not evident grossly unless observed using the fluorescent imaging technique (Case 1 in Table 2). (A) Preoperative contrast enhanced computed tomography (CT) revealed 2 hypervascular tumors in Couinaud's segment I (arrow and arrowhead). (B) On the resected specimens, fluorescent imaging identified 2 fluorescing lesions corresponding to the lesions identified on the preoperative CT (left), although only the larger 1 (arrow) was identifiable by gross examination (right). (C) When the smaller fluorescing lesion (arrowhead) was cut deeper after formalin fixation, cancerous tissues with a diameter of 2 mm appeared (arrow). (D) Microscopically, the smaller tumor proved to be a moderately differentiated hepatocellular carcinoma (silver reticulin stain, original magnification, ×40).
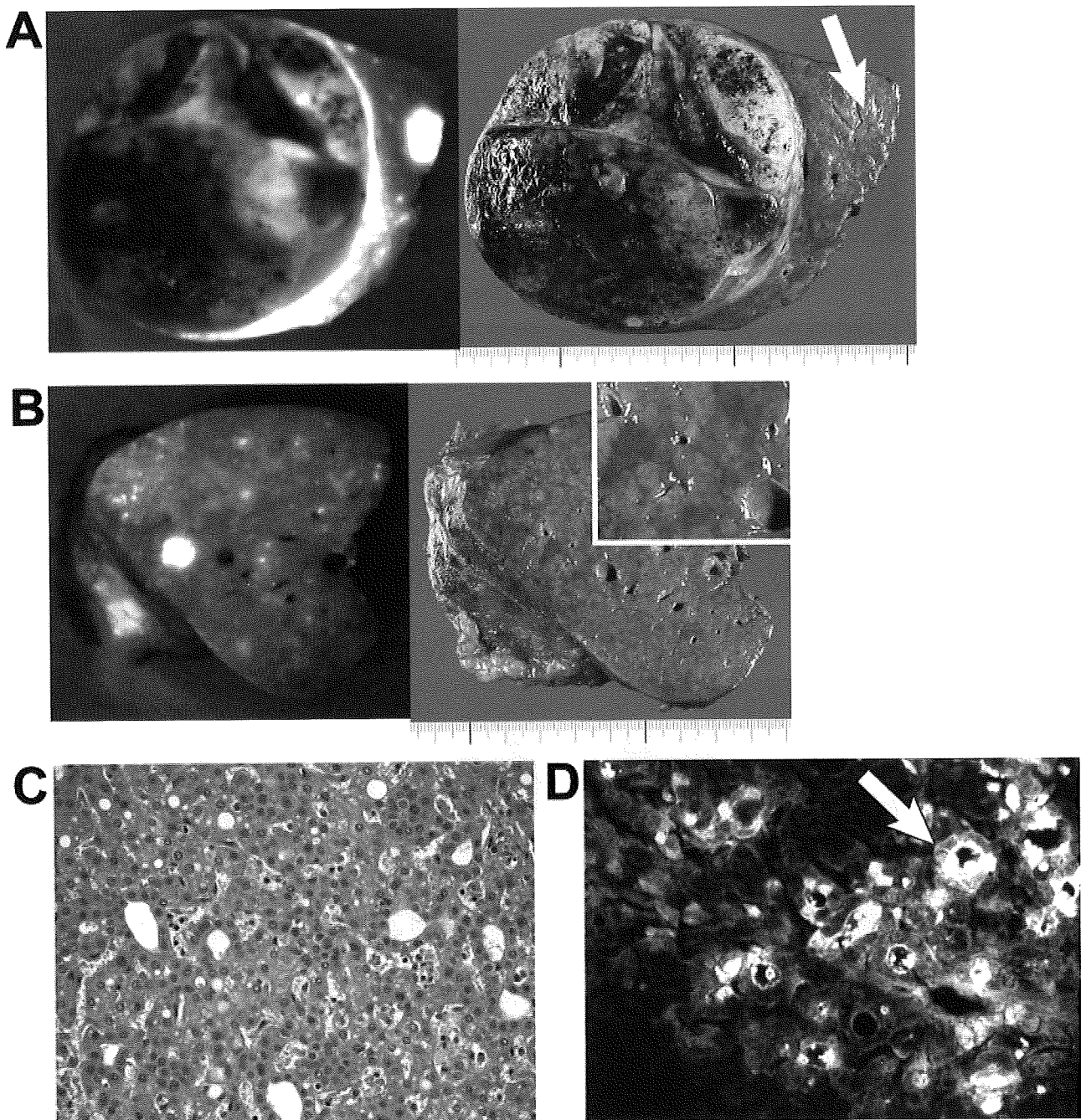
FIGURE 2. Early hepatocellular carcinomas that were detected using the fluorescent imaging technique (Case 5 in Table 2). (A) Fluorescent imaging (left) delineated a fluorescing lesion at a site where no cancerous lesion had been grossly identified (arrow on right side). Fluorescence was also demonstrated in the viable cancer tissues of the main tumor and in liver parenchyma compressed by the tumor. (B) Fluorescent imaging detected another grossly unidentifiable lesion apart from the main tumor (inset shows a magnified view of the lesion on gross examination). (C) Microscopic examinations revealed early hepatocellular carcinomas comprising well-differentiated cancer cells with little cellular and structural atypia and pseudogland formation in both of the 2 fluorescing lesions (H&E, originally × 40). (D) Fluorescent microscopy confirmed the origin of the fluorescence in the cancer cell cytoplasm and pseudoglands (arrow).

Total fluorescent type

Partial fluorescent type
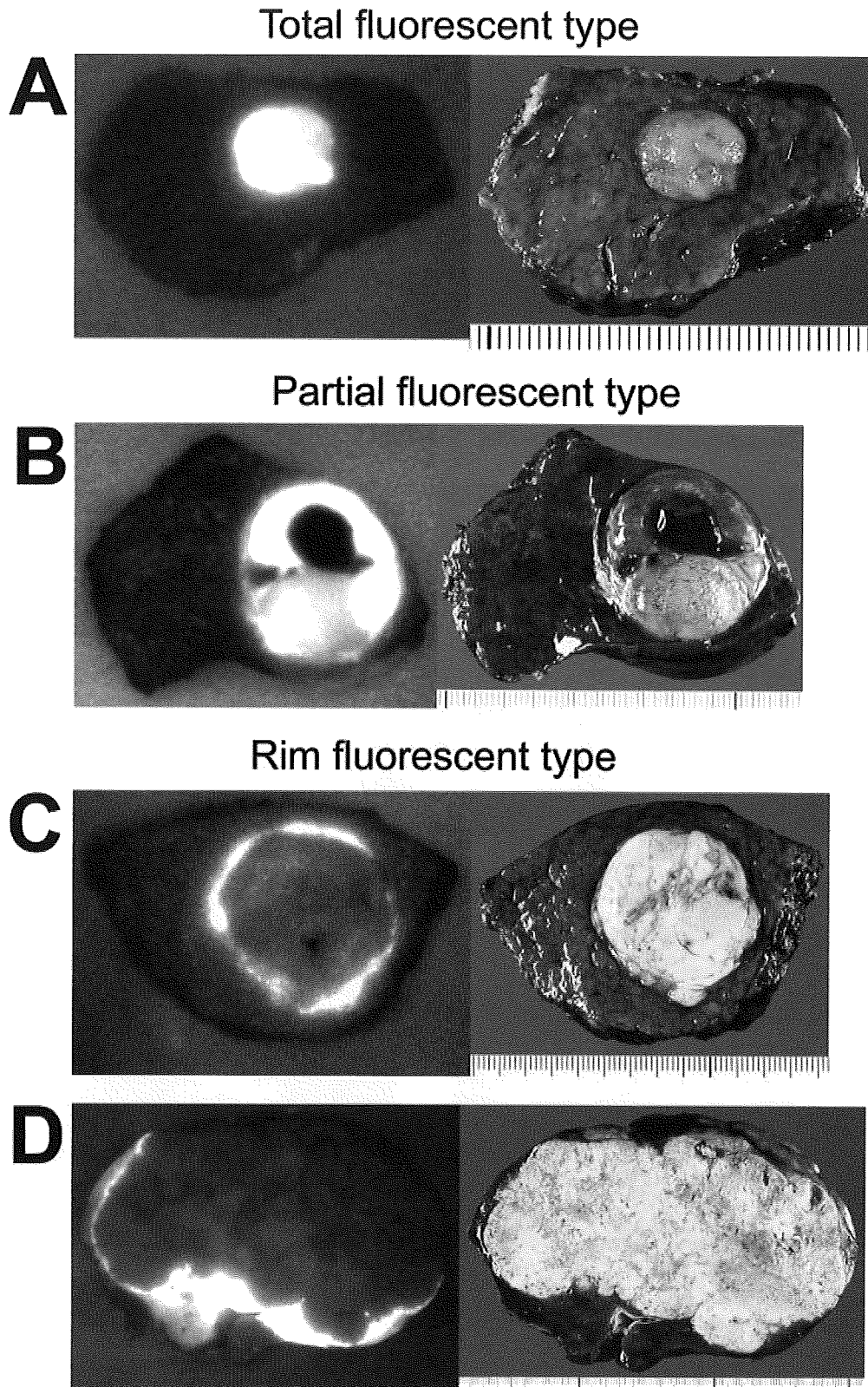

Rim fluorescent type

FIGURE 3. Fluorescent patterns of liver cancers on surgical specimens (left) and their gross appearances (right). (A) Total fluorescent type; well-differentiated hepatocellular carcinoma (HCC), 7 mm in diameter. (B) Partial fluorescent type; moderately differentiated HCC with well-differentiated components and hemorrhagic necrosis at the upper half of the tumor, 36 mm in diameter. (C) Rim fluorescent type; poorly differentiated HCC, 30 mm in diameter. (D) Rim fluorescent type; metastasis of colon carcinoma, 130 mm in diameter.

Table 3. Fluorescent Patterns of HCCs*

Variable	Total Fluorescent Type, n=33	Partial Fluorescent Type, n=26	*P*
ICG retention rate at 15 min (%)†	16.2 (4.3-46.5)	10.2 (3.7-23.4)	.056
Interval from ICG injection to surgery			
Within 24 h	5 (15%)	4 (15%)	>.999
More than 24 h	28 (85%)	22 (85%)	
Tumor size (mm)†	12 (2-40)	30 (7-150)	<.001
Cancer cell differentiation			
Well	19 (58%)	0 (0%)	<.001
Moderate or poor	14 (42%)	26 (100%)	
Early HCC	11 (33%)	0 (0%)	.001
Pseudoglands			
Present	28 (85%)	13 (50%)	.005
Absent	5 (15%)	13 (50%)	

HCC indicates hepatocellular carcinoma; ICG, indocyanine green.
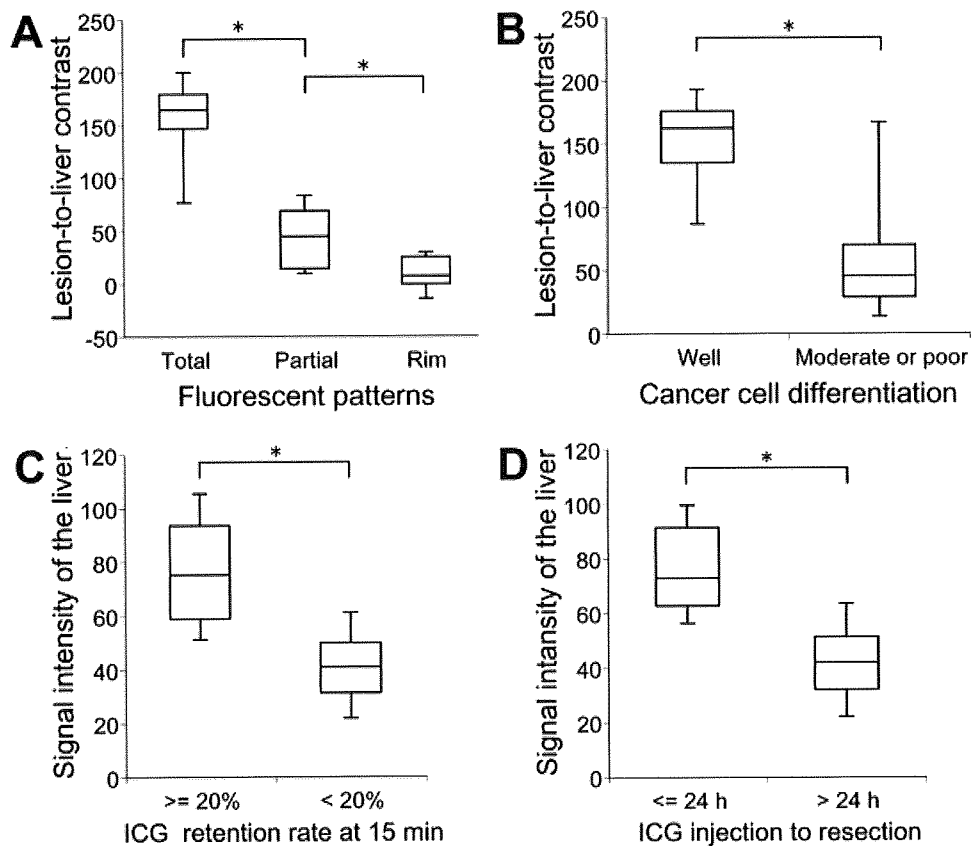*Excluding 4 HCCs classified as rim-fluorescent type.
†Median with range.

FIGURE 4. Signal intensity assessment. (A) Lesion-to-liver contrast among total fluorescent type (n = 33), partial fluorescent type (n = 26), and rim fluorescent type (n = 32) tumors. (B) Lesion-to-liver contrast between well-differentiated (n = 19) and moderately or poorly differentiated (n = 44) hepatocellular carcinoma. (C) Signal intensity of the noncancerous liver parenchyma around the tumors, which were classified according to the patients' indocyanine green (ICG) retention rate at 15 minutes (equal to or greater than 20%, n = 14; less than 20%, n = 77). (D) Signal intensity of the noncancerous liver parenchyma around the tumors, which were classified according to the intervals between the ICG injection and resection (equal to or shorter than 24 hours, n = 10; longer than 24 hours, n = 81). Boxes reflect the median (2fifth-7fifth percentile). The horizontal bars show the limits of the 10th and 90th percentiles and the asterisk indicates *P* < .001.
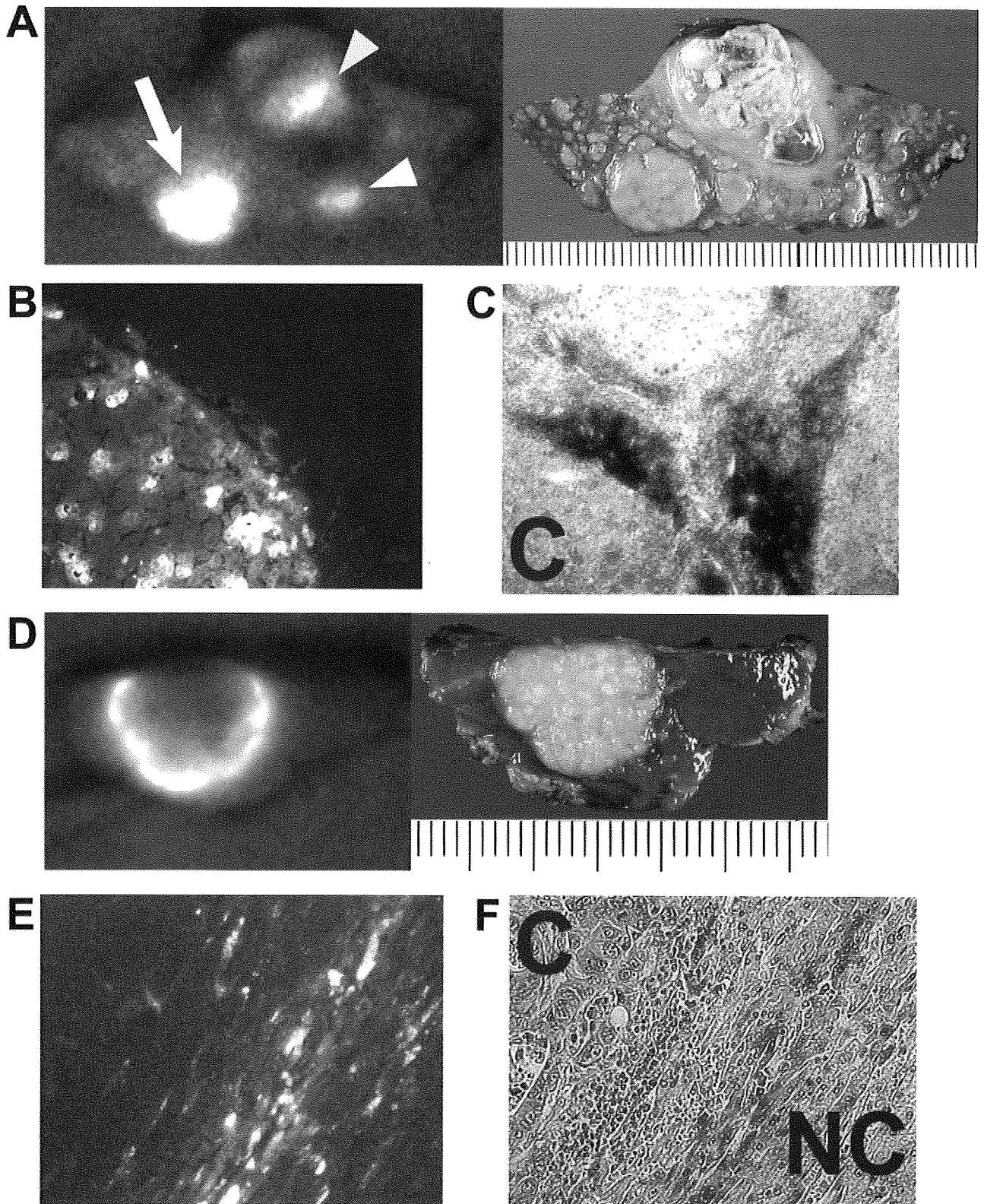
FIGURE 5. Fluorescent microscopic imaging of hepatocellular carcinoma (HCC) and metastasis of colorectal carcinoma (CRC). HCC (Case 3 in Table 2): (A) Fluorescent imaging revealed fluorescence in the newly detected well-differentiated HCC (arrow in left) as well as in a viable component of the moderately differentiated HCC (yellow arrowhead) and in a large regenerative nodule (white arrowhead). (B) Fluorescent microscopy showed fluorescence only in the cancer cell cytoplasm and pseudoglands (originally × 40). (C) A merged image of the fluorescence (demonstrated in red) on a hematoxylin-stained cross section confirmed fluorescence in the cancer tissues (C) but not in the surrounding noncancerous liver tissues (originally × 10). CRC metastasis: (D) Fluorescent imaging revealed a fluorescing rim around a tumor. (E) Fluorescent microscopic image (originally × 10). (F) A merged image of the fluorescence (demonstrated in red) on a hematoxylin-stained cross section confirmed that fluorescence was emitted not from the cancer tissues (C) but from the surrounding noncancerous liver tissues (NC) compressed by the tumor.
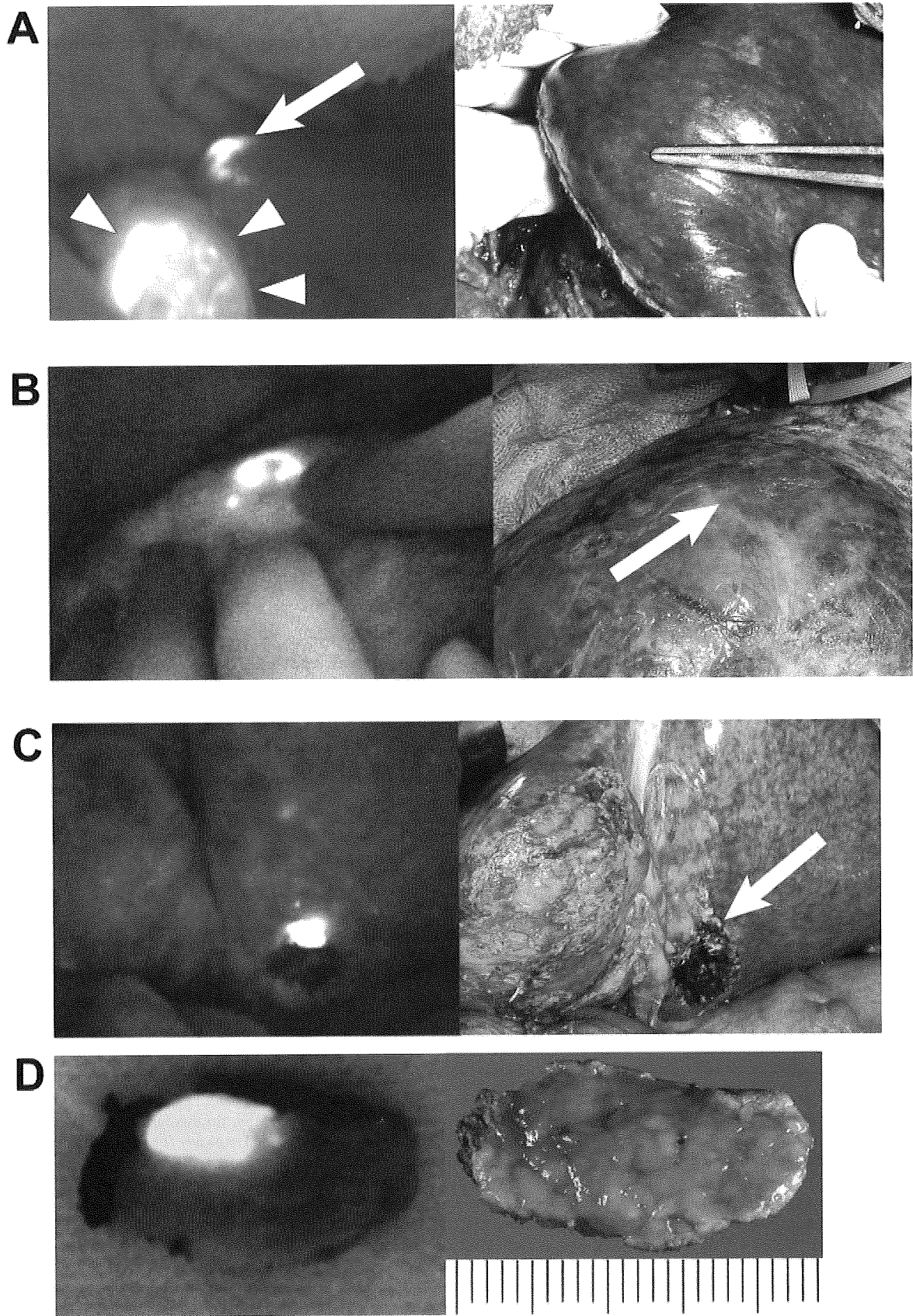
FIGURE 6.

Signal Intensity Assessment on Fluorescent Images

The lesion-to-liver contrast was significantly higher among the total fluorescent-type tumors (165^{54-218} per pixel) than among the partial fluorescent-type tumors (45 [-6-87] per pixel, $P < .001$) and was also higher among the partial fluorescent-type tumors than among the rim fluorescent-type tumors (7 [-25-45] per pixel, $P < .001$; Fig. 4A). Among the 63 HCCs, well-differentiated cancers were associated with a significantly higher lesion-to-liver contrast than moderately or poorly differentiated cancers (163^{71-218} per pixel vs 68 [-6-211] per pixel, $P < .001$; Fig. 4B). The signal intensity of the noncancerous liver parenchyma was significantly higher among patients with an ICG retention rate at 15 minutes of equal to or greater than 20% compared with those with an ICG retention rate at 15 minutes of less than 20% (75^{46-107} per pixel vs 41^{12-91} per pixel, $P < .001$; Fig. 4C), and it was also higher among patients in whom ICG had been injected within 24 hours before surgery than among those in whom the ICG had been injected more than 24 hours before surgery (73^{56-105} per pixel vs 42^{12-107} per pixel, $P < .001$; Fig. 4D).

Fluorescent Microscopy

Fluorescent microscopy confirmed the presence of fluorescence in the cytoplasm and pseudoglands of the HCC cells in areas where the ICG-fluorescent imaging of the surgical specimens had demonstrated fluorescence (Fig. 2D and Fig. 5A-C). In the rim fluorescence type-HCCs and metastases, the fluorescence was confirmed to exist not in the cancerous tissues, but in the surrounding noncancerous liver tissues where the cellular density had been increased as a result of compression by the tumor (Fig. 5D-F).

Cancer Detection by Using ICG-Fluorescent Imaging Before Resection

ICG-fluorescent imaging technique also identified 21 of the 41 HCCs that were examined (51%, Fig. 6A) and all of the 16 CRC metastases (Fig. 6B) on the liver surfaces before resection. Among the 20 tumors that were not identified by intraoperative ICG-fluorescent imaging, the tumor size was smaller than that of the 37 identifiable tumors (11^{2-40} mm vs 18^{3-130} mm, $P = .019$) and the tumor location was deeper (10^{3-35} mm vs 2^{0-8} mm, $P < .001$). When the 41 HCCs and the 16 metastases were compared, the locations of the HCCs were significantly deeper than those of the metastases (5^{0-35} mm vs 1^{0-6} mm, $P < .001$), while the tumor size of the HCCs (12^{2-102} mm) was not different from that of the metastases (18^{7-130} mm, $P = .471$). None of the tumors at a depth of more than 8 mm from the liver surfaces were identifiable.

Intraoperative ultrasonography revealed 33 of the 41 HCCs (80%) and all of the 16 metastases. Among the remaining 8 HCCs that were unidentifiable by intraoperative ultrasonography, ICG-fluorescent imaging on the liver surfaces detected 3 HCCs located at a depth of 1-2 mm from the liver surfaces.

In 1 patient with HCC (Case 4 in Table 2), intraoperative fluorescent imaging after resection demonstrated residual cancer tissues, which were unidentifiable by gross examination or intraoperative ultrasonography, on the raw surface of the remnant liver, requiring an additional resection to be performed (Fig. 6C, D).

DISCUSSION

ICG-fluorescent imaging identified all of the microscopically confirmed HCCs and CRC liver metastases in the surgical specimens. Well-differentiated HCCs were

---

FIGURE 6. Fluorescent images of cancers on liver surfaces before resection. (A) Intraoperative fluorescent imaging clearly identified a hepatocellular carcinoma (HCC) on the liver surface (arrow) that was not visible or palpable (tumor location was determined by intraoperative ultrasonography and is indicated by the tweezers). A cross section of the tumor is demonstrated in Figure 3A. The transverse colon was also fluorescing (arrowheads) as a result of indocyanine green in the stool. (B) A rim-fluorescing metastasis was delineated on the liver surface (its cross section was shown in Fig. 5D). Palpation of the tumor was difficult because of the presence of thick connective tissues on the liver surface from a previous surgery. (C) Intraoperative fluorescent imaging revealed that a fluorescing lesion remained on the raw surface of the remnant liver after resection (left), although the lesion was not identified by gross examination or manual palpation (right). The residual fluorescing lesion was in addition resected. (D) A cross section of the in addition resected liver specimen. Fluorescent imaging confirmed the presence of the lesion (left), which was still unidentifiable by gross examination of the cut surface. Subsequent microscopic examinations revealed an early HCC in the fluorescing area.

---

detected as uniformly and highly fluorescing lesions, while poorly differentiated HCCs and metastases of CRC were detected as rim-fluorescing lesions with a low lesion-to-liver contrast. Microscopically, fluorescence was confirmed to originate in the cytoplasm and pseudoglands of HCC cells and in the noncancerous liver parenchyma surrounding poorly differentiated HCCs and metastases. These results suggest that well- or moderately differentiated HCC produces tumorous fluorescence because the cancer tissues retain the portal uptake of ICG despite the functional and/or architectural destruction of biliary excretion due to cancer progression. In contrast, poorly differentiated HCCs and metastases produce rim fluorescence probably because of biliary excretion disorders in the surrounding noncancerous liver tissues that have been compressed by the tumor. Such mechanisms for the ICG-fluorescent imaging of liver cancers are consistent with those for delayed (10-24 hours) magnetic resonance imaging using biliary-excreted contrast material, which can be used to demonstrate tumorous hyperenhancement in well-differentiated HCCs and rim enhancement in metastases.[21-24]

The major expected role of ICG-fluorescent imaging in clinical settings is the identification of small liver cancers, especially early HCC, which have been shown to be the earliest clinical entity of HCC and to have a high cure rate.[7,9,10] Theoretically, our fluorescent imaging technique could be used to delineate any lesions retaining ICG in surgical specimens cut into 10-mm sections because near-infrared light penetrates human tissues to a depth of about 5-10 mm.[25] Indeed, 8 of the 63 HCCs (13%) in our series were not evident grossly unless observed by ICG-fluorescent imaging because of their deep tumor locations and/or indistinct tumor margins. Furthermore, 5 of the 11 early HCCs (45%) were macroscopically detectable only by fluorescent imaging. These results indicate that ICG-fluorescent imaging enables the highly sensitive identification of small liver cancers on surgical specimens, enhancing the accuracy of operative cancer staging. This technique may also rewrite the incidence of early HCC and provide new aspects for research on hepatocarcinogenesis.[26-29]

ICG-fluorescent imaging was also useful for identifying liver cancers before resection: 51% of the HCCs and all of the CRC metastases were delineated on the liver surfaces. Although the reason for the lower detectability of the HCCs compared with the metastases is not totally clear, cancer detectability using this technique seems mainly to depend on the depth of the tumors from the liver surface because of the limited tissue penetration of near-infrared light,[25] as described earlier, rather than the characteristics of the cancerous tissues. Indeed, none of the tumors at a depth of more than 8 mm from the liver surfaces were identifiable in our series. Despite this limitation in detecting deeply located cancers, however, intraoperative ICG-fluorescent imaging is still useful because it not only aids visual inspections and palpation, but it also compensates for drawbacks in intraoperative ultrasonography in observing small lesions located just beneath the liver surface. Furthermore, this technique can be used to detect residual cancerous tissues on the raw surface of the remnant liver after resection (Fig. 6C, D). With the future application of fluorescent imaging systems to laparoscopes, ICG-fluorescent imaging may become an indispensable means of identifying liver cancers during laparoscopic hepatectomies,[30,31] in which surgeons cannot palpate the liver surface.

Other advantages of our ICG-fluorescent technique are its safety and feasibility. ICG is already used worldwide to evaluate liver function before resection. The reported incidence of adverse reactions after the intravenous injection of ICG is quite small (approximately 0.003%).[15] Furthermore, our fluorescent imaging technique can use the ICG that is injected for routine liver function tests. Once ICG is administered within 14 days before surgery, we can obtain fluorescent images of liver cancers in real time by simply placing the camera imaging head on the liver surface or on surgical specimens.

Our study has several limitations. First, our results indicated that the signal intensity of the noncancerous liver parenchyma was higher in patients with an unfavorable ICG retention rate and in patients who had received the ICG injection within 24 hours before surgery. These findings suggest that the interval between the ICG injection and surgery should be longer than at least 2 days to obtain a good lesion-to-liver contrast, especially in patients with advanced cirrhosis. Further studies are needed to determine the optimal dosage of ICG for fluorescent imaging based on the patient's liver function. Second, ICG-fluorescent imaging revealed 5 false-positive lesions in our HCC series. The incidence and characteristics of false-positive lesions should be clarified in larger

study populations, although the presented techniques are already useful in clinical settings for the intraoperative identification of lesions suspected of being cancerous.

In conclusion, ICG-fluorescent imaging can be used to observe HCC lesions based on their tumorous fluorescence because the portal uptake of ICG is preserved in well- or moderately differentiated cancer tissues, despite the lack of biliary extraction, and to delineate poorly differentiated HCC and CRC metastases as rim-fluorescing lesions because of biliary excretion disorders in the surrounding noncancerous liver tissues that are compressed by the tumor. Our fluorescent imaging technique enables the highly sensitive identification of small and grossly unidentifiable liver cancers in real time, enhancing the accuracy of liver resection and operative cancer staging.

Conflict of Interest Disclosures

References

1. Sahani DV, Kalva SP, Tanabe KK, et al. Intraoperative US in patients undergoing surgery for liver neoplasms: comparison with MR imaging. *Radiology*. 2004;232:810-814.

2. Zhang K, Kokudo N, Hasegawa K, et al. Detection of new tumors by intraoperative ultrasonography during repeated hepatic resections for hepatocellular carcinoma. *Arch Surg*. 2007;142:1170-1175.

3. Machi J, Isomoto H, Kurohiji T, et al. Accuracy of intraoperative ultrasonography in diagnosing liver metastasis from colorectal cancer: evaluation with postoperative follow-up results. *World J Surg*. 1991;15:551-556.

4. Leen E, Ceccotti P, Moug SJ, et al. Potential value of contrast-enhanced intraoperative ultrasonography during partial hepatectomy for metastases: an essential investigation before resection? *Ann Surg*. 2006;243:236-240.

5. Nomura K, Kadoya M, Ueda K, Fujinaga Y, Miwa S, Miyagawa S. Detection of hepatic metastases from colorectal carcinoma: comparison of histopathologic features of anatomically resected liver with results of preoperative imaging. *J Clin Gastroenterol*. 2007;41:789-795.

6. Kanai T, Hirohashi S, Upton MP, et al. Pathology of small hepatocellular carcinoma. A proposal for a new gross classification. *Cancer*. 1987;60:810-819.

7. Takayama T, Makuuchi M, Hirohashi S, et al. Early hepatocellular carcinoma as an entity with a high rate of surgical cure. *Hepatology*. 1998;28:1241-1246.

8. Liver Cancer Study Group of Japan. Classification of primary liver cancer. 4th ed. Tokyo: Kanehara; 2001.

9. Kojiro M, Roskams T. Early hepatocellular carcinoma and dysplastic nodules. *Semin Liver Dis*. 2005;25:133-142.

10. Llovet JM, Burroughs A, Bruix J. Hepatocellular carcinoma. *Lancet*. 2003;362:1907-1917.

11. Rubens FD, Ruel M, Fremes SE. A new and simplified method for coronary and graft imaging during CABG. *Heart Surg Forum*. 2002;5:141-144.

12. Balacumaraswami L, Abu-Omar Y, Choudhary B, Pigott D, Taggart DP. A comparison of transit-time flowmetry and intraoperative fluorescence imaging for assessing coronary artery bypass graft patency. *J Thorac Cardiovasc Surg*. 2005;130:315-320.

13. Landsman ML, Kwant G, Mook GA, Zijlstra WG. Light-absorbing properties, stability, and spectral stabilization of indocyanine green. *J Appl Physiol*. 1976;40:575-583.

14. Ishizawa T, Tamura S, Masuda K, et al. Intraoperative fluorescent cholangiography using indocyanine green: a biliary road map for safe surgery. *J Am Coll Surg*. 2009;208:e1-e4.

15. Cherrick GR, Stein SW, Leevy CM, Davidson CS. Indocyanine green: observations on its physical properties, plasma decay, and hepatic extraction. *J Clin Invest*. 1960;39:592-600.

16. Ishizawa T, Hasegawa K, Aoki T, et al. Neither multiple tumors nor portal hypertension are surgical contraindications for hepatocellular carcinoma. *Gastroenterology*. 2008; 134:1908-1916.

17. Makuuchi M, Hasegawa H, Yamazaki S. Ultrasonically guided subsegmentectomy. *Surg Gynecol Obstet*. 1985;161: 346-350.

18. Kokudo N, Bandai Y, Imanishi H, et al. Management of new hepatic nodules detected by intraoperative ultrasonography during hepatic resection for hepatocellular carcinoma. *Surgery*. 1996;119:634-640.

19. Makuuchi M, Kosuge T, Takayama T, et al. Surgery for small liver cancers. *Semin Surg Oncol*. 1993;9:298-304.

20. International Working Party. Terminology of nodular hepatocellular lesions. *Hepatology*. 1995;22:983-993.

21. Ni Y, Marchal G, Yu J, et al. Experimental liver cancers: Mn-DPDP-enhanced rims in MR-microangiographic-histologic correlation study. *Radiology*. 1993;188: 45-51.

22. Coffin CM, Diche T, Mahfouz A, Alexandre M, Caseiro-Alves F, Rahmouni A. Benign and malignant hepatocellular tumors: evaluation of tumoral enhancement after mangafodipir trisodium injection on MR imaging. *Eur Radiol*. 1999;9:444-449.

23. Wang DB, Zhou KR, Zeng MS, Chen KM, Wang YX. Mn-DPDP-enhanced 24-h delayed-scan MRI of hepatocellular carcinoma is correlated with histology. *Eur Radiol*. 2004;14:743-745.

24. Chung JJ, Kim MJ, Kim KW. Mangafodipir trisodium-enhanced MRI for the detection and characterization of

focal hepatic lesions: is delayed imaging useful? *J Magn Reson Imaging.* 2006;23:706-711.

25. Kim S, Lim YT, Soltesz EG, et al. Near-infrared fluorescent type II quantum dots for sentinel lymph node mapping. *Nat Biotechnol.* 2004;22:93-97.

26. Takayama T, Makuuchi M, Hirohashi S, et al. Malignant transformation of adenomatous hyperplasia to hepatocellular carcinoma. *Lancet.* 1990;336:1150-1153.

27. Terasaki S, Kaneko S, Kobayashi K, Nonomura A, Nakanuma Y. Histological features predicting malignant transformation of nonmalignant hepatocellular nodules: a prospective study. *Gastroenterology.* 1998;115:1216-1222.

28. Nam SW, Park JY, Ramasamy A, et al. Molecular changes from dysplastic nodule to hepatocellular carcinoma through gene expression profiling. *Hepatology.* 2005;42:809-818.

29. Llovet JM, Chen Y, Wurmbach E, et al. A molecular signature to discriminate dysplastic nodules from early hepatocellular carcinoma in HCV cirrhosis. *Gastroenterology.* 2006;131:1758-1767.

30. Gagner M, Rheault M, Dubuc J. Laparoscopic partial hepatectomy for liver tumor. *Surg Endosc.* 1992;6:97-98.

31. Belli G, Fantini C, D'Agostino A, et al. Laparoscopic versus open liver resection for hepatocellular carcinoma in patients with histologically proven cirrhosis: short- and middle-term results. *Surg Endosc.* 2007;21:2004-2011.

NADPH Oxidase 4 Contributes to Transformation Phenotype of Melanoma Cells by Regulating G2-M Cell Cycle Progression

Maki Yamaura,[1] Junji Mitsushita,[2] Shuichi Furuta,[2] Yukiko Kiniwa,[1] Atsuko Ashida,[1] Yasuhumi Goto,[1] Wei H. Shang,[2] Makoto Kubodera,[2] Masayoshi Kato,[2] Minoru Takata,[1] Toshiaki Saida,[1] and Tohru Kamata[2]

Departments of [1]Dermatology and [2]Molecular Biology and Biochemistry, Shinshu University Graduate School of Medicine, Matsumoto, Nagano, Japan

Abstract

Generation of reactive oxygen species (ROS) has been implicated in carcinogenic development of melanoma, but the underlying molecular mechanism has not been fully elucidated. We studied the expression and function of the superoxide-generating NADPH oxidase (Nox)4 in human melanoma cells. Nox4 was up-regulated in 13 of 20 melanoma cell lines tested. Silencing of Nox4 expression in melanoma MM-BP cells by small interfering RNAs decreased ROS production and thereby inhibited anchorage-independent cell growth and tumorigenecity in nude mice. Consistently, a general Nox inhibitor, diphenylene iodonium, and antioxidants vitamine E and pyrrolidine dithiocarbamate blocked cell proliferation of MM-BP cells. Flow cytometric analysis indicated that Nox4 small interfering RNAs and diphenylene iodonium induced G2-M cell cycle arrest, which was also observed with another melanoma cell line, 928mel. This was accompanied by induction of the Tyr-15 phosphorylated, inactive form of cyclin-dependent kinase 1 (a hallmark of G2-M checkpoint) and hyperphosphorylation of cdc25c leading to its increased binding to 14-3-3 proteins. Ectopic expression of catalase, a scavenger of ROS, also caused accumulation of cells in G2-M phase. Immunohistochemistry revealed that expression of Nox4 was detected in 31.0% of 13 melanoma patients samples, suggesting the association of Nox4 expression with some steps of melanoma development. The findings suggest that Nox4-generated ROS are required for transformation phenotype of melanoma cells and contribute to melanoma growth through regulation of G2-M cell cycle progression. [Cancer Res 2009;69(6):2647–54]

Introduction

A growing body of evidence indicates that reactive oxygen species (ROS) generated by NADPH oxidase (Nox) family enzymes [Nox1-5 and dual oxidases (Duox1 and 2)] play critical roles in various physiologic processes in *Caenorhabditis elegans* as well as mammals (1). These include innate immunity, cell growth, and apoptosis. For example, Nox1 mediates angiotensin II–induced proliferation of vascular smooth muscle cells (2) and platelet-derived growth factor– or epidermal growth factor–dependent mitogenesis of nonphagocytic cells (3, 4). Nox4 is integrated into the receptor systems for insulin-induced glucose transport (5) and lipopolysaccharide-stimulated inflammation (6). The NADPH oxidase consists of multiple subunits including a Nox family protein, the catalytic moiety homologous to phagocytic gp91phox, and regulatory proteins. It catalyzes reduction of molecular oxygen to produce superoxide and its metabolite, hydrogen peroxide.

It has been known that ROS are spontaneously generated in malignant cancer cells, but their origin and biological meaning remained obscured (7). Recent studies revealed some aspects of the functional relationships between Nox family genes and increased ROS production in tumor cells. Nox1-generated ROS are functionally required for oncogenic Ras transformation phenotype including anchorage-independent growth and tumorigenesis (4, 8). Nox4 contributes to cell survival of pancreatic cancer cells, and this survival signaling seemed to be mediated by the impared activities of AKT and its target ASK1 (9, 10). Nox5 has also been implicated in cell viability of prostate cancer cells (11) and Barrett esophageal adenocarcinoma cells (12).

Melanoma is one of the aggressive tumors with a high frequency of metastasis and malignancy in melanoma cells is often accompanied by elevated ROS production through multiple mechanisms (13). Overexpression of the antioxidant enzyme, superoxide dismutase, suppresses the ability of melanoma cells to form colonies in soft agar as well as tumors in nude mice (14). The dietary antioxidant, tocopherol (vitamine E), induces growth inhibition of melanoma cells (15). These observations imply that redox alterations play an important role in the carcinogenic evolution of melanoma. With the respect to involvement of Nox isozymes in these ROS productions, Nox1 has been implicated in acute ROS formation in human kerationcytes elicited by UV A radiation (16), whose role in development of cutanous melanoma is still being debated. Recently, Nox4 expression was reported to be constitutively up-regulated and partially account for the elevated ROS production in some of melanoma cell lines (17), but the Nox4 action has not been fully elucidated. In the present study, we describe that ablation of Nox4 expression by RNA interference blocks both proliferation of melanoma cells and tumorigenesis derived from melanoma cells in athymic nude mice. This growth inhibition seems to be a consequence of inhibition of G2-M cell cycle transition, which is associated with increased phosphorylation of cyclin-dependent kinase 1 (CDK1), a key mitosis-promoting kinase and hyperphosphorylation of cdc25c. Furthermore, up-regulated expression of Nox4 was detected in some of melanoma samples isolated from patients. Our finding suggests that Nox4-generated ROS exert a mediating role in melanoma cell growth by regulating G2-M cell cycle progression and for the first time

— 94 —

provides evidence of the involvement of Nox enzymes in cell cycle control.

Materials and Methods

Cell culture and materials. A variety of human melanoma cell lines were obtained from different sources (see Supplementary Table S1) and maintained in DMEM supplemented with 10% fetal bovine serum (FBS). A human epidermal melanocyte cell line was obtained from Cascade Biologics and maintained in Medium 254 (Cascade Biologics) with HMGS (Cascade Biologics). Propidium iodide, 6-hydroxy-2, 5, 7,8-tetramethylchroman-2-carboxylic acid (a water-soluble vitamine E analogue), rabbit anticatalase antibodies, and monoclonal anti-p21$^{WAF1/C2P1}$ antibodies were purchased from Sigma; PDTC, diphenyleneiodonium (DPI), and rabbit anti-phospho CDK1 (tyr-15) antibodies from Calbiochem; and AEC substrate chromagen and horseradish peroxidase (HRP)-conjugated anti-rabbit IgG antibodies from DAKO. Rabbit anti-cdc25c antibodies were purchased from Cell Signaling and rabbit anti-p53 (FL-393) and rabbit anti–14-3-3 antibodies from Santa Cruz. Human Nox4 cDNAs were subcloned into pEGFP-C1 vectors (Clontech) containing Green Fluorescent Protein (GFP-hNox4).

Transfection and siRNA constructions. Transfection was carried out by using Lipofectamine 2000 (Invitrogen) according to the manufacturer's protocol. DNA oligonucleotides encoding siRNA with loop sequence (TTCAAGAGA) were subcloned into the H1 promoter vector, pSilencer hygro (Ambion). Nox4 siRNAs were designed as follows: 5′-CAGAA-CATTCCATATTAC-3′ for siNox4-1 and 5′-ACTTTGTTGAACTGAATG-3′ for siNox4-2, respectively. All of the constructs were verified by sequencing. A scrambled siRNA plasmid (Ambion) encodes hairpin siRNA whose sequence is not found in the human genome databases.

Isolation of stable transfectants. pSilencer vectors carrying siNox4-1, siNox4-2, and scrambled siRNA (1 μg) were transfected into MM-BP cells (10^6). Transfected cells were subjected to selection in DMEM supplemented with 10% FBS and 400 μg/mL hygromycin for 2 wk. Isolated colonies were maintained in the presence of 100 μg/mL hygromycin. The presence of stably transfected vectors in the cells was confirmed by PCR using vector-specific primers. We referred to the two cell lines carrying pSilencer siNox4-1 as siRNA1-a and siRNA1-b, a cell line carrying pSilencer siNox4-2 as siRNA2, and a cell line carrying pSilencer scrambled siRNA as scrambled.

Reverse transcription-PCR and real-time PCR. Total RNAs (5 μg) were extracted from cells with TRIzol (Invitrogen) and reverse-transcribed by Power Script (Clonetech) with Oligo dT primers (Invitrogen). The resultant cDNA was PCR amplified for human NOX1-5 by using human sense and antisense primers:

sense 5′-GGAGCAGGAATTGGGGTCAC-3′ and antisense 5′-TTGCTGTCCCATCCGGTGAG-3′ for Nox1; sense 5′-GGAGTTTCAAGATGCGTGGAAACTA-3′ and antisense 5′-GCCAGACTCAGAGTTGGAGATGCT-3′ for Nox2; sense 5′-GGATCGGAGTCACTCCCTTCGCTG-3′ and antisense 5′-ATGAACACCTCTGGGGTCAGCTGA-3′ for Nox3; sense 5′-CTCAGCGGAATCAATCAGCTGTG-3′ and antisense 5′-AGAGGAACACGACAATCAGCCTTAG-3′ for Nox4; sense 5′-ATCAAGCGGCCCCCTTTTTTTCAC-3′ and antisense 5′-CTCATTGTCACACTCCTCGACAGC-3′ for Nox5

Nox4 expression in various melanoma cell lines was evaluated with real-time PCR (35 cycles) using Taqman Gene Expression assay (Applied Biosystems) with glyceraldehyde-3-phosphate dehydrogenase as an internal control.

Growth curve. Cells (10^4) were grown in the presence or absence of antioxidants and DPI, and the numbers of live cells were determined by trypan blue exclusion. Alternatively, cells were inoculated and labeled with [^{3}H] thymidine (0.1 μCi; GE Healthcare) in the presence or absence of the above chemicals. Labeled cells were precipitated with 10% chilled trichloroacetic acid for 10 min, and the incorporated radioactivity was determined by nitrocellulose filtration, followed by scintillation counting.

Soft agar assay. The assay was performed as described previously (4). The appearance of colonies was monitored for up to 12 d. The numbers of colonies larger than 4 mm were counted.

Immunoblotting. Cells were lysed in radioimmunoprecipitation assay buffer [PBS, 0.1% SDS, 1% Na-deoxycholate, 1% Triton X-100, 50 mmol/L NaF, 1 mmol/L sodium orthovanadate, 10 mmol/L sodium PPi leupeptin (10 μg/mL), pepstatin A (10 μg/mL), and phenylmethylsulfonyl fluoride (1 mmol/L)]. Extracted proteins were separated by SDS-PAGE and subjected to immunoblotting with indicated antibodies.

Tumorigenecity analysis. To determine tumor formation by each transfected cell line, trypsinized cells (10^7) were suspended in 0.2 mL of PBS, and the cell suspensions were inoculated s.c. into athymic mice. All of the animals were observed for the formation of tumors for up to 3 wk. The size of tumor was measured at the 12th day with an external caliper, and volume was calculated.

Preparation of anti-Nox4 antibodies. The COOH-end peptides of Nox4 (CLSNQNNSYGTRFFYNKESFS) cross-linked to keyhole limpet hemocyanin

Table 1. A summary of histochemical study

Patient	Age	Sex	Primary lesion	Sample	Clinical type	Nox4 expression
1	69	M	Foot	Primary	ALM	Positive
2	83	M	Finger	Primary	ALM	Negative
3	69	F	Foot	Primary	ALM	Positive
4	61	F	Foot	Primary	ALM	Negative
5	76	M	Finger	Primary	ALM	Negative
6	68	F	Lower leg	Primary	SSM	Positive
7	48	F	Rt. arm	LN meta	SSM	Negative
8	76	M	Head	LN meta	SSM	Negative
9	67	M	Upper back	Primary	SSM	Positive
10	85	M	Neck	Primary	SSM	Negative
11	64	F	Lower leg	Primary	SSM	Negative
12	53	F	Abdomen	Primary	NM	Negative
13	63	F	Genital Mucosa	LN meta	mucosal	Negative

NOTE: Melanoma tissues isolated from patients were processed for immunohistochemistry using anti-Nox4 antibodies as described in Materials and Methods.

Abbreviations: ALM, acral lentiginous melanoma; rt. arm, right arm; LN, lymphnode; SSM, superficial spreading melanoma; NM, nodular melanoma.
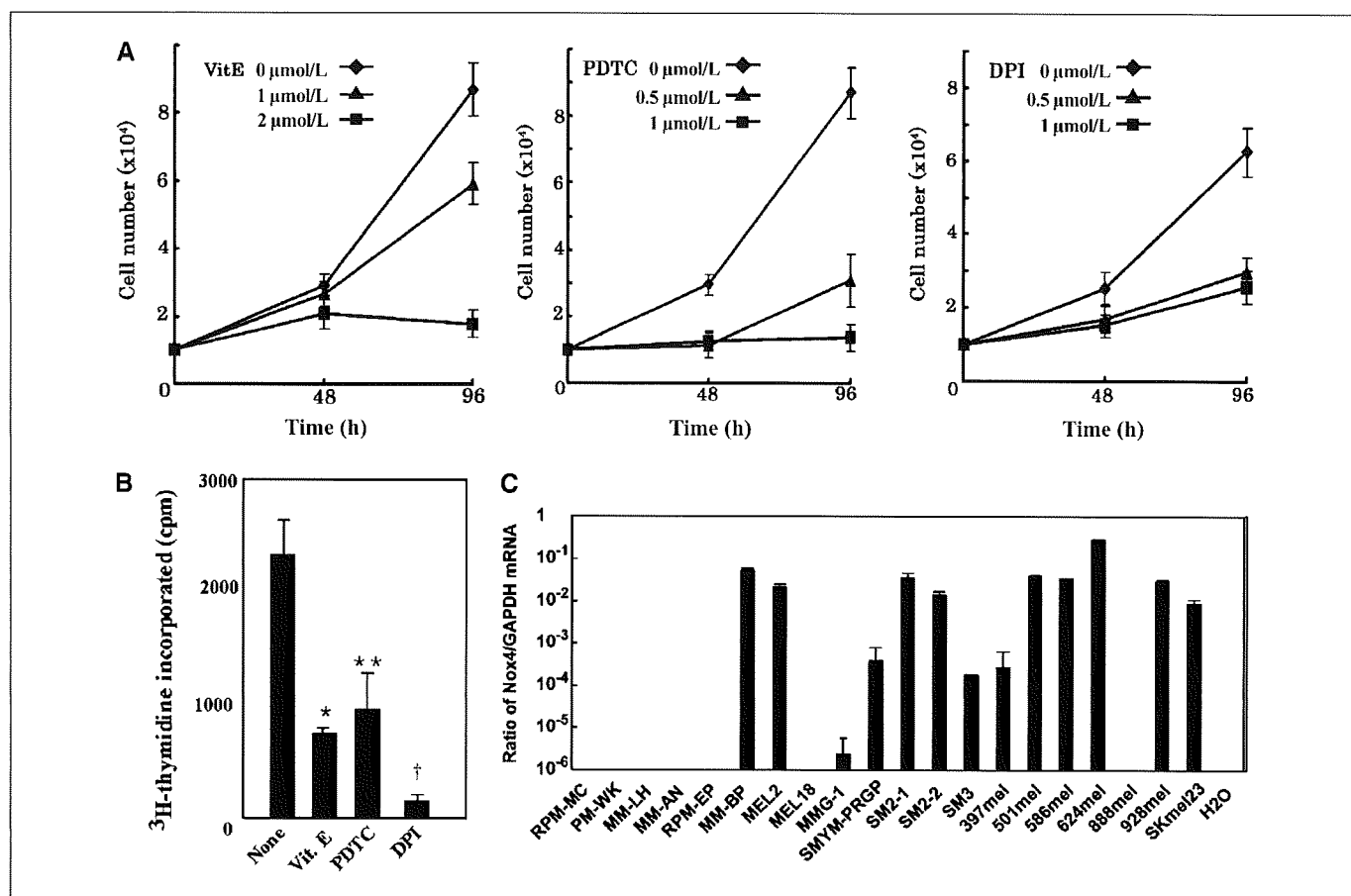
— 95 —

Figure 1. Effect of antioxidants and DPI on MM-BP cell growth and Nox4 expression in melanoma cell lines. A, cells were cultured in the presence or absence of vitamine E, PDTC, and DPI until live cells were harvested at the indicated times and the number of live cells was determined. Points, mean in triplicated dishes; bars, SD. B, alternatively, MM-BP cells (10^5) were metabolically labeled with [^{3}H]thymidine for 48 h in the presence of 2 μmol/L vitamine E, 1 μmol/L PDTC, or 1 μmol/L DPI. The radioactivity incorporated were determined. Columns, mean ($n = 4$); bars, SD. P^*, P^{**}, and $P^+ < 0.05$ versus none. C, The levels of Nox4 expression in various melanoma cell lines were examined by real-time PCR. Columns, mean of duplicated assays; bars, SD.

were immunized into rabbits, and the antiserum was affinity purified. In some experiments, mouse monoclonal antibodies against Nox4 (gift by Dr. B. Goldstein, Department of Medicine, Jefferson Medical College, Thomas Jefferson University, Philadelphia, PA) were used.

Measurement of intracellular ROS. Forty-eight hours after plating, cells were incubated with HBSS (Invitrogen) containing 10 μmol/L 2;7'-dichlorodihydrofluorescein diacetate (Molecular Probes) for 10 min at 37°C. Images were obtained with a Zeiss confocal microscope. Fluorescence was quantitated on an arbitrary unit and the data represent the fluorescence intensity of ~50 random cells obtained from three separate fields.

Determination of the cellular DNA content by fluorescence-activated cell sorting analysis. MM-BP cells were plated at 1×10^5 cell density per 60-mm dish, starved for 48 h in DMEM containing 0.5% serum, and then maintained for 48 h in DMEM containing 10% serum. Trypsinized cells (10^6–10^7) were subjected to cell cycle analysis using propidium iodide as described (18). Relative DNA content of nuclei was measured by a fluorescence-activated cell sorter (Becton Dickinson).

Immunohistochemistry. Primary or metastatic melanoma tissues were obtained from informed patients. Immunohistochemistry was performed on 4-μm thick formalin-fixed paraffin-embedded tissue. Paraffin sections were dewaxed in xylene and rehydrated with distilled water. The tissue sections were activated in Tris-EDTA buffer (pH 9) in the microwave oven for 25 min. The slides were subsequently incubated with the purified rabbit anti-human Nox4 antibody, followed by HRP-conjugated anti-rabbit IgG antibodies. For controls, the antibodies preadsorbed with Nox4 peptide antigens were used. Staining was visualized with AEC substrate chromogen,

followed by hematoxylin counterstaining. Indirect immunofluorescence staining was performed and samples were observed under a confocal microscope (LSM510; Carl Zeiss) as described previously (8).

Statistical analysis. The statistical analysis was performed with Student's t test. For multiple treatment groups, a factorial ANOVA followed by Bonferroni's t test was applied. Differences with P values of <0.05 were considered to be statistically significant.

Results

Effects of antioxidants and DPI on melanoma cell growth. To explore the functional role of ROS-generating enzymes in malignant melanoma, we first examined whether proliferation of melanoma cells requires ROS production. Human melanoma MM-BP cells (19) were treated with increasing amounts of a dietary antioxidant vitamine E and a thiol-containing antioxidant pyrrolidine dithiocarbamate (PDTC). Consistent with other reports (15), vitamine E decreased the growth of MM-BP cells in liquid culture (Fig. 1A) and PDTC was also effective in inhibiting the cell growth (Fig. 1A). Furthermore, DPI, a flavoprotein-dependent oxidase inhibitor, showed the growth inhibitory effect (Fig. 1A), whereas rotenone, a mitochondrial oxidase inhibitor, had little or no effect (data not shown). The inhibitory effects of vitamine E, PDTC, and DPI were also confirmed by cell proliferation assay using [^{3}H] thymidine incorporation (Fig. 1B). These results suggest that Nox

— 96 —

family enzymes participate in growth control involving ROS in MM-BP cells. To further study the source of ROS generation, we examined the expression of Nox family mRNAs in MM-BP cells. Reverse transcription-PCR analysis revealed that a relatively high amount of Nox4 mRNA was expressed in MM-BP cells compared with other Nox family homologues including Nox1, Nox2, Nox3, and Nox5 (Fig. 2A). No appreciable Nox4 messages were detected in melanocytes under the condition used (Fig. 2A). In addition, real-time PCR showed that significant levels of Nox4mRNA were expressed in 13 of 20 melanoma cell lines with different origins (Supplementary Table S1; Fig. 1C). Accordingly, it is conceivable that up-regulation of Nox4 is not a particular characteristics of MM-BP cells but a frequent event among melanoma cell lines. In the subsequent study, we therefore focused on the Nox4 action in MM-BP cells.

Nox4 is involved in ROS generation in melanoma cells. To probe the functional role of Nox4 in melanoma, we stably transfected the expression vectors carrying siRNAs for Nox4 into MM-BP cells. With the isolated clones, RT-PCR and immuno-blotting analysis showed that loading with siRNA1 or siRNA2

significantly decreased the amounts of Nox4 mRNAs (Fig. 2A) and Nox4 proteins (the data for a cell line, siRNA1-b, are not shown; Fig. 2A) compared with those in the scrambled siRNA preparation, which indicated that introduced Nox4 siRNAs effectively repressed the Nox4 expression. To test whether Nox4 mediates intracellular ROS production, generation of H_2O_2, a dismutated metabolite of Nox4-derived superoxide was measured in Nox4siRNA-transfected cell lines after addition of the fluorescent oxidant indicator dye 2;7'-dichlorodihydrofluorescein diacetate. Although intracellular DCF fluorescence was detected in scrambled siRNA-transfected MM-BP cells, this fluorescence was sharply attenuated in siRNA1-a, siRNA1-b, and siRNA2 cells (Supplementary Fig. S1; Fig. 2B). The results indicate that Nox4 siRNAs inhibit spontaneous oxidant generation in MM-BP cells, suggesting the involvement of Nox4 in ROS production in melanoma cells.

Effects of Nox4 siRNAs on melanoma proliferation. Because DPI or antioxidants treatment blocked proliferation of MM-BP cells (Fig. 1A–D), we next examined whether suppression of the Nox4 activity by Nox4siRNAs induces dysregulation of cell proliferation. Soft agar assay as an *ex vivo* model of tumorigenicity shows
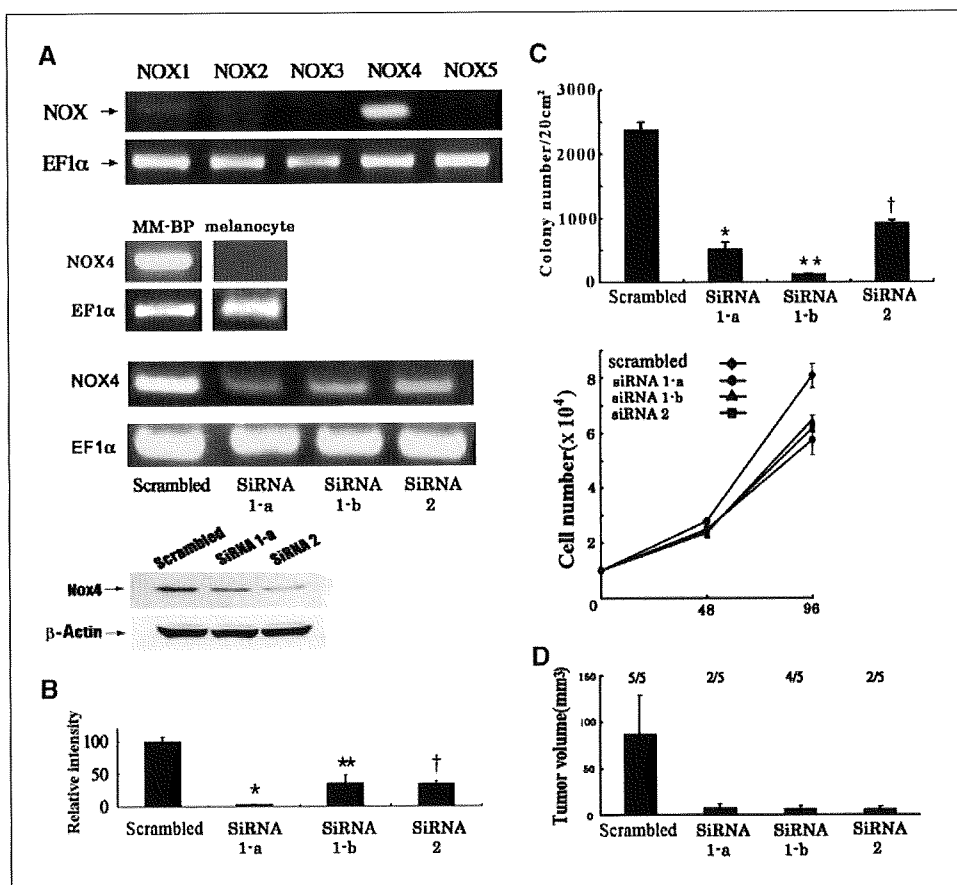

Figure 2. mRNA expression of Nox family members in MM-BP cells and suppression of Nox4 expression by Nox4 siRNAs. *A,* total RNAs were extracted from MM-BP cells and mRNA expressions of Nox isoforms were analyzed by RT-PCR with EFIα expression as internal controls (*top*). RT-PCR was performed with melanocyte and MM-BP cells. Total RNAs were extracted from the cell lines carrying scrambled siRNA or Nox4-specific siRNAs (*1-a, 1-b,* or *2*) and RT-PCR, with EF1αmRNA as a control, was performed to analyze Nox4 mRNA expression (*middle*). Alternatively, lysates (10⁶ cells) prepared from these cell lines were subjected to immunoblotting with mouse monoclonal anti-Nox4 antibodies (*top*) or anti-βactin antibodies (*bottom*). *B,* Nox4siRNAs inhibit production of ROS in MM-BP cells. The cell lines (10⁷cells) carrying Nox4siRNAs or scrambled siRNA were loaded with 2;7'-dichlorodihydrofluorescein diacetate for 10 min. ROS generation was detected by a confocal microscope. *Columns,* mean of three separate experiments (arbitrary unit); *bars,* SD. *P**, *P***, and *P*⁺ < 0.05 versus scrambled. *C,* anchorage-independent cell growth on soft agar (*top*). The cell lines were seeded in soft agar and colonies were scored. *Columns,* mean of separate experiments (*n* = 3); *bars,* SD. *P**, *P***, and *P*⁺ < 0.05 versus scrambled. Cell proliferation in liquid culture (*bottom*). The cell numbers were determined at the indicated time points. *Points,* mean of three separate experiments; *bars,* SD. *D,* tumor formation by cell lines carrying Nox4 siRNAs. Each cell lines were injected into nude mice, and tumor volume was measured; *columns,* mean; *bars,* SD. Fraction numbers show the ratio of the mice bearing tumors to the total mice used.